


Cite this: *Mater. Adv.*, 2022,  
3, 3457

# A one-pot strategic construction of functionalized nanomaterial ZIF-90-Rhn for stepwise detection and capturing of Ag<sup>+</sup> and formaldehyde from an aqueous solution†

Xiaoyu Du,<sup>a</sup> Mengwen Li,<sup>a</sup> Man Du,<sup>\*b</sup> Ao Shen,<sup>a</sup> Xiaohui Hao,<sup>a</sup> Jiaxin Yuan,<sup>a</sup>  
Shufeng Ma,<sup>a</sup> Yongwei Zhao,<sup>a</sup> Lala Hou,<sup>a</sup> Ziqi Li<sup>a</sup> and Yunxu Yang  <sup>\*a</sup>

In this work, a new functionalized nanomaterial, **ZIF-90-Rhn**, was designed, synthesized and characterized. The synthesis was performed by one-pot strategic construction, post-modification and pre-modification synthesis methods. After encapsulating cyanine dye, Cy-N, into **ZIF-90-Rhn**, a multi-functional complex of **ZIF-90-Rhn@Cy-N** was successfully obtained and could be used to detect Ag<sup>+</sup> in dual-signals (fluorescence signal and visual color signal) by forming an intermedial product of **ZIF-90-Rhn@Ag<sup>+</sup>/Cy-N** in an aqueous solution. Subsequently, the intermediate product **ZIF-90-Rhn@Ag<sup>+</sup>/Cy-N** could detect formaldehyde (FA) via a stepwise redox recognition reaction through dual-signals. A smartphone portable online detection platform for Ag<sup>+</sup> and FA using Bluetooth for the color changes under visible light was not realized, and the results are consistent with the fluorescence sensing assay results. Moreover, a chitosan non-woven fabric coated with **ZIF-90-Rhn@Cy-N** on its surface was considered to evaluate its efficient capturing and removing effects on Ag<sup>+</sup> and FA in a stepwise actual procedure in water.

Received 17th January 2022,  
Accepted 16th February 2022

DOI: 10.1039/d2ma00047d

rsc.li/materials-advances

## 1. Introduction

Heavy metal ions are not biodegradable and tend to accumulate in organisms, and their beneficial or detrimental effect is concentration-dependent. Heavy metal ions have toxic effects on the human body and increase the risk of cancer.<sup>1</sup> Among heavy metal ions, Ag<sup>+</sup> has been discharged in the environment in large quantities via industrial wastes and emissions every year; this has led to serious environmental pollution and affected the production safety of food and agriculture.<sup>2,3</sup> When the concentration of Ag<sup>+</sup> in drinking water is higher than 0.9 μM, it will be toxic to the human body and can cause damage to the brain and even the immune system.<sup>4,5</sup> Therefore, detecting the trace amount of Ag<sup>+</sup> in the environment and industrial samples in time and effectively is extremely important. Nowadays, typical techniques for detecting Ag<sup>+</sup> include atomic absorption spectrometry (AAS), inductively coupled plasma mass spectrometry (ICP-MS), optical emission spectrometry (OES), and voltammetry,<sup>6,7</sup> but there are deficiencies such as complicated

sample pretreatment steps or expensive instruments. However, fluorescent probes have attracted considerable attention because of their high sensitivity, high selectivity, short response time and easy real-time monitoring.

Because of the structure of the activated formyl group, formaldehyde (FA) is one of the biologically-active strong substances and will not only pollute the environment but also cause irritation to the eyes and nose, parts of the human body, damage the central nervous system, cause immune system disorders and respiratory system diseases, and is one of the main carcinogens in the human body.<sup>8–10</sup> Current FA detection methods depend on gas chromatography,<sup>11–13</sup> high-performance liquid chromatography<sup>14</sup> and spectroscopy,<sup>15,16</sup> which are highly selective and sensitive but are time-consuming and require expensive testing equipment and technicians.

In the past few decades, nanomaterials, such as functionalized MOFs, have been the subject of extensive research. They were developed appropriately to many practical applications such as sensing, catalysis, biomedicine, gas storage, hydrogen storage, and drug delivery, green chemical *etc.*<sup>17–21</sup> due to their high designability, the high specific surface area of the flexible, tunable porosity and morphology. Various luminescent MOFs have been extensively developed for the detection of ions, gas molecules, solvents, dyes and explosives.<sup>22</sup> Moreover, MOFs such as MIL-121<sup>23</sup> and ZIF-67<sup>24</sup> are one of the ideal platforms, and have been developed and utilized in diversified fluorescent forms for

<sup>a</sup> Department of Chemistry and Chemical Engineering, School of Chemistry and Biological Engineering, University of Science and Technology Beijing, Beijing 100083, China. E-mail: yxyang@ustb.edu.cn

<sup>b</sup> School of Chemical and Pharmaceutical Engineering, Hebei University of Science and Technology, Shijiazhuang, 050018, China

† Electronic supplementary information (ESI) available. See DOI: 10.1039/d2ma00047d

$\text{Ag}^+$  capture and removal. Nano-fluorescent probe technology can quickly and specifically identify FA in a porous nano-system, such as UIO-66- $\text{NH}_2$ ,<sup>25</sup> Al-MIL-53- $\text{N}_2\text{H}_2$ ,<sup>26</sup> ZIF-8,<sup>27</sup> ZIF-90-LW,<sup>28</sup> and Ag-MOFs.<sup>29</sup> Therefore, designing and developing new efficient nano-fluorescence probes to realize the detection of  $\text{Ag}^+$  and FA with convenient equipment, simple operation and easy signal identification has considerable significance.

Generally, MOFs can be functionalized by introducing different functional groups in their organic components. When the guests of specific ions or molecules enter the channel or cavity of MOFs to interact with the ligand functional groups, metal sites, or the doped molecules, the fluorescent properties of nano-functionalized MOFs would change and thus achieve the fluorescence assay of specific substrate molecules. The development of functionalized MOFs involves multiple strategies and methods.<sup>30,31</sup> By mixing guests and precursors of MOFs in one-pot with certain strictly controlling of various parameters (temperature, solvent concentration ratio, surfactant, etc.),<sup>32–37</sup> a homogeneous complex can be formed rather than a discrete structure. So, one-pot synthesis *in situ* packaging is one of the simplest fabrication methods of MOFs compared to the pre-modification and post-modification synthesis strategies.

With the above information in mind, herein, we designed and synthesized a functionalized nanomaterial **ZIF-90-Rhn** using one-pot strategic *in situ* synthesis construction. The post-modification of MOFs or the pre-modification of ligands can be performed and could stepwise detect and capture  $\text{Ag}^+$  and FA from the aqueous solution. The logic for the detection of  $\text{Ag}^+$  and FA by stepwise recognition reactions is based on the following design: (1) Using a synthetic strategy, such as one-pot generation, **ZIF-90-Rhn** was synthesized using imidazole-2-carboxaldehyde (ICA),  $\text{Zn}^{2+}$  with rhodanine-3-acetic acid (**Rhn**) *in situ*. **ZIF-90-Rhn** should demonstrate certain characteristics of acidity and the ability to provide carboxyl protons because of the carboxyl groups in **Rhn**. **ZIF-90-Rhn** could bind with the secondary amine of heptamethine cyanine (**Cy-N**,  $\lambda_{\text{em}} = 722 \text{ nm}$ ). Although there was no fluorescence of its own, **ZIF-90-Rhn** could synchronize and quench the fluorescence of **Cy-N** as cyanine was doped in the pores and formed a non-fluorescence **ZIF-90-Rhn@Cy-N** complex. (2) Based on the synergism of carboxyl and thioketone groups in **Rhn** of **ZIF-90-Rhn**, **ZIF-90-Rhn** could recognize and coordinate with  $\text{Ag}^+$  to form **ZIF-90-Rhn@Ag<sup>+</sup>**.<sup>38</sup> Thus, the addition of  $\text{Ag}^+$  destroyed the **ZIF-90-Rhn@Cy-N** complex and simultaneously followed the formation of **ZIF-90-Rhn@Ag<sup>+</sup>**, thus resulting in the liberation of free **Cy-N** with the consequent restoration of the fluorescent emission of **Cy-N**. Finally, the recognition system demonstrate an enhanced fluorescent intensity because of the generation of **ZIF-90-Rhn@Ag<sup>+</sup>/Cy-N**. (3) When FA encountered the new system of **ZIF-90-Rhn@Ag<sup>+</sup>/Cy-N**, the unique redox activity of FA induced a reduction reaction and transformed  $\text{Ag}^+$  to  $\text{Ag}^0$ . Thus, the redox destroyed the coordination of **ZIF-90-Rhn@Ag<sup>+</sup>** after sequential addition of FA and freed or restored the proton providing capacity of carboxyl functional groups of **ZIF-90-Rhn** again. The new combination of

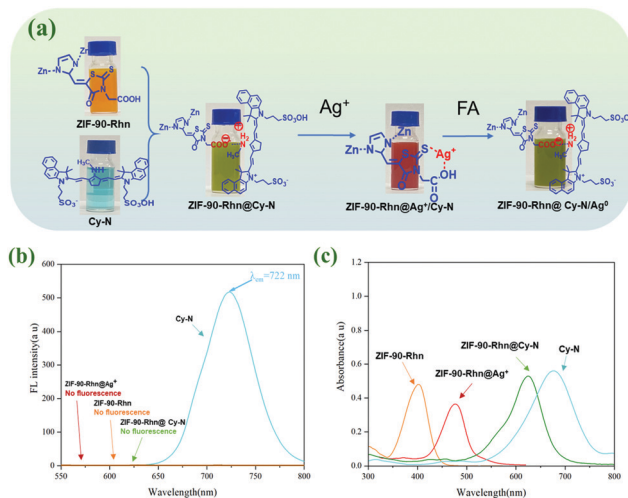


**Fig. 1** (a) Schematic representation of **ZIF-90-Rhn@Cy-N** for  $\text{Ag}^+$  and FA sensing. (The colors of all compounds were presented in ethanol solution.) (b) The fluorescence spectra of **ZIF-90-Rhn**, **ZIF-90-Rhn@Ag<sup>+</sup>**, **ZIF-90-Rhn@Cy-N** and **Cy-N** (100  $\mu\text{M}$  respectively),  $\lambda_{\text{ex}} = 678 \text{ nm}$ . (c) UV-vis spectra of **ZIF-90-Rhn**, **ZIF-90-Rhn@Ag<sup>+</sup>**, **ZIF-90-Rhn@Cy-N** and **Cy-N**.

**ZIF-90-Rhn** and **Cy-N** resulted in the rebuilding of the non-fluorescent **ZIF-90-Rhn@Cy-N** complex too.

To our delight, from the continuous step by step recognitions of  $\text{Ag}^+$  and FA, there were interesting visual color changes that were accompanied except for the mentioned stepwise changes of fluorescence signals in the system (Fig. 1). As **ZIF-90-Rhn** (orange) was mixed with **Cy-N** (ultramarine), a new grass-green complex of **ZIF-90-Rhn@Cy-N** was produced. With the addition of  $\text{Ag}^+$  to the complex, the grass-green complex of **ZIF-90-Rhn@Cy-N** changed to a new brick-red **ZIF-90-Rhn@Ag<sup>+</sup>/Cy-N** mixture. A return change to the grassy green of **ZIF-90-Rhn@Cy-N** complex was then followed with the addition of FA (Fig. 1a). So, a dual signal (fluorescent signal and visual color signal) of **ZIF-90-Rhn@Cy-N@Ag<sup>+</sup>/FA** was observed as the stepwise detecting and removal of  $\text{Ag}^+$  and FA were performed (Fig. 1b and c). The results indicated great utilization potentiality in environmental monitoring and pollutant removal for  $\text{Ag}^+$  and FA.

## 2. Experimental section

### 2.1. Materials and instrumentations

The details are shown in the ESI.<sup>†</sup>

### 2.2. Synthesis

**2.2.1. Synthesis of ZIF-90-Rhn (a) by one-pot of *in situ*.** A mixture of imidazole-2-carboxaldehyde (ICA) (0.096 g, 1 mmol), rhodanine-3-acetic acid (**Rhn**) (0.21 g, 1.1 mmol) and  $\text{Zn}(\text{NO}_3)_2 \cdot 6\text{H}_2\text{O}$  (0.147 g, 0.5 mmol) was refluxed in methanol (50 mL) with triethylamine (5 mL) for 8 h at 80 °C to obtain a yellow solid product. Consecutively, the yellow product was washed with methanol until the filtrate was colorless and transparent, and then the products were dried overnight in a vacuum at 110 °C and afforded **ZIF-90-Rhn** (a) (0.368 g, 92%).



**2.2.2. Synthesis of ZIF-90-Rhn (b) by post-modification.** Zn ( $\text{NO}_3$ )<sub>2</sub>·6H<sub>2</sub>O (0.371 g, 1.25 mmol) was added to 12.5 mL propan-2-ol as a triggered solvent, which was subsequently added to deionized water (12.5 mL) with ICA (0.48 g, 5 mmol) and PVP (0.5 g) to form a typical H<sub>2</sub>O/propan-2-ol/polyvinylpyrrolidone (PVP) mixture system. The resulting powder was stirred for a few minutes at room temperature. Finally, the as-obtained products were collected by centrifugation (12 000 rpm), washed with excess methanol, and vacuum dried at 50 °C to obtain **ZIF-90**. Subsequently, the mixture of **ZIF-90** (0.23 g, 1 mmol) and **Rhn** (0.21 g, 1.1 mmol) was refluxed in ethanol (50 mL) with pyridine (0.079 g, 1 mmol) for 8 h at 80 °C to obtain a yellow solid product. The solid products were washed with ethanol and dried in vacuum to obtain **ZIF-90-Rhn (b)** (1.520 g, 76%).

**2.2.3. Synthesis of ZIF-90-Rhn (c) by pre-modification of ligands.** **ZIF-90-Rhn (c)** was synthesized according to a previously reported synthesis method.<sup>39</sup> A mixture of ICA (0.096 g, 1 mmol) and rhodanine-3-acetic acid (0.21 g, 1.1 mmol) was refluxed in ethanol (50 mL) with pyridine (0.079 g, 1 mmol) for 4 h at 80 °C to obtain a yellow solid product, and then the solid products were washed with ethanol and dried in a vacuum to obtain **ligand 1**. Consecutively, the new crystalline ZIF structure of **ZIF-90-Rhn (c)** was synthesized by heating the solution mixture of **ligand 1** and Zn ( $\text{NO}_3$ )<sub>2</sub>·6H<sub>2</sub>O (3 : 2 mol ratio) in DMF at 100 °C for 18 h (0.248 g, 62%).

**2.2.4. Generation of ZIF-90-Rhn@Cy-N.** **ZIF-90-Rhn@Cy-N** was prepared as per the following procedure. The solution of **ZIF-90-Rhn** (0.4 g, 1 mmol) in 10 mL of methanol and **Cy-N** (0.62 g, 1 mmol) solution in 5 mL of methanol were mixed in a bottle and stirred at room temperature. After 4 h of reaction, the green product was centrifuged and dried.

**2.2.5. ZIF-90-Rhn@Cy-N for Ag<sup>+</sup> sensing.** For each test, **ZIF-90-Rhn@Cy-N** dispersion solution (100 μM) was mixed with different concentrations of Ag<sup>+</sup> (0–120 μM). The fluorescence spectra of these solutions were collected in the wavelength range from 600 to 800 nm ( $\lambda_{\text{ex}}$  = 678 nm).

**2.2.6. ZIF-90-Rhn@Ag<sup>+</sup>/Cy-N for FA sensing.** For each test, the **ZIF-90-Rhn@Ag<sup>+</sup>/Cy-N** dispersion solution (the concentrations of **ZIF-90-Rhn@Ag<sup>+</sup>/Cy-N** are 100 μM) was mixed with different concentrations of FA (0–30 μM) solutions. The experimental data of the two signals (fluorescence signal and visual color signal) were tested in turn. The fluorescence spectra of these solutions were collected in the wavelength range from 600 nm to 800 nm ( $\lambda_{\text{ex}}$  = 678 nm).

**2.2.7. The experiment tests on colors (R/G value) under visible light.** The color titration experiment was performed under visible light. The smartphone and spectrophotometer formed a portable test platform to read the data. Once the spectrophotometer's camera captured the sample color (**ZIF-90-Rhn@Cy-N** for Ag<sup>+</sup> or **ZIF-90-Rhn@Ag<sup>+</sup>/Cy-N** for FA), the smartphone would immediately display the sample colors and display the R (red), G (green) and B (blue) values of the samples. For each test, **ZIF-90-Rhn@Cy-N** dispersion in ethanol (100 μM) was mixed with different concentrations of Ag<sup>+</sup> (10–100 μM), and the colors of the samples were imaged and analyzed. In the same way, **ZIF-90-Rhn@Ag<sup>+</sup>/Cy-N** dispersion in

the ethanol system (100 μM/100 μM) was mixed with different concentrations of FA (1–25 μM) solutions, and the colors of the samples were imaged and analyzed.

**2.2.8. The experiment tests about time-dependence of ZIF-90-Rhn@Cy-N for Ag<sup>+</sup> or ZIF-90-Rhn@Ag<sup>+</sup>/Cy-N for FA.** In the experimental study of **ZIF-90-Rhn@Cy-N** response time, Ag<sup>+</sup> (100 μM) was added to **ZIF-90-Rhn@Cy-N** dispersion in ethanol (100 μM), and the emission intensity at 722 nm was collected from 30 s to 600 s under  $\lambda_{\text{ex}}$  = 678 nm, and the color changes at different moments were recorded. Then the time dependence of **ZIF-90-Rhn@Ag<sup>+</sup>/Cy-N** dispersion in ethanol system (100 μM/100 μM) for FA was performed. After the abovementioned addition of Ag<sup>+</sup> to **ZIF-90-Rhn@Cy-N** dispersion in ethanol (100 μM) and finally for 600 s, FA (25 μM) was added to the mixture of **ZIF-90-Rhn@Ag<sup>+</sup>/Cy-N** dispersion in ethanol system (100 μM/100 μM), and the emission intensity at 722 nm was obtained from 630 s to 1200 s under  $\lambda_{\text{ex}}$  = 678 nm, and the color changes at different moments were recorded.

### 3. Results and discussion

#### 3.1. The synthesis of the functionalized nano-material of ZIF-90-Rhn

The post-modified synthesis is the best modification method to ensure the original morphology of a MOFs material, while pre-modified construction is the best modification method to ensure its really chemical structure. So, considering the advanced nature of one-pot for synthesis *in situ* tactics, **ZIF-90-Rhn (a)** was first synthesized by the one-pot synthesis process *in situ*, then we speculated that the pore size of **ZIF-90-Rhn (a)** was ~3.55 nm (Fig. S5, ESI<sup>†</sup>), which was suitable for certain guest molecules to be doped in. Moreover, to confirm the chemical structure and the original morphology of this tentatively synthesized **ZIF-90-Rhn (a)**, a post-modified condensation reaction of **Rhn** and **ZIF-90** was adopted to synthesize **ZIF-90-Rhn (b)** in order to maintain the morphology structural features of **ZIF-90**. Then, the organic **ligand 1** was synthesized by condensation reaction between **Rhn** and ICA; a pre-modification of **ligand 1** was used to synthesize **ZIF-90-Rhn (c)** using a thermal solution method with Zn<sup>2+</sup> (as shown in Scheme 1a–c). The synthesis of **ZIF-90-Rhn (b)** by post-modified method and **ZIF-90-Rhn (c)** by pre-modified method were proved and compared, and similarity, homogeneity and characteristics were the same as **ZIF-90-Rhn (a)** and **ZIF-90** contributing to the structural morphology.

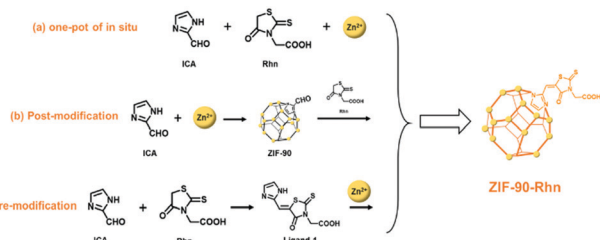
#### 3.2. Characterization of ZIF-90-Rhn a, b, c

The structural characterization of **ZIF-90**, including FT-IR spectra, PXRD, SEM, and XPS, were reported.<sup>40–42</sup> The morphology characterization of **ZIF-90-Rhn (a–c)** was performed using the following structural characterization methods.

First, FT-IR measurements on ICA, **Rhn** and **ZIF-90-Rhn (a)** were performed as shown in Fig. 2. The aldehydic carbonyl of ICA appeared at 1685 cm<sup>−1</sup>, the shift of carbonyl (–COOH, –RN–CO) and thione (–C=S) in **Rhn** appeared at 1720 cm<sup>−1</sup>, 1624 cm<sup>−1</sup> and 1197 cm<sup>−1</sup>. The characteristic peaks of carbonyl (–COOH,







**Scheme 1** The synthetic route of **ZIF-90-Rhn**. (The end product through *in situ* synthesis was named **ZIF-90-Rhn** (a), the end product through post-modification was named **ZIF-90-Rhn** (b), the end product through pre-modification was named **ZIF-90-Rhn** (c).)

–RN–CO), thione (–C=S) and C=C groups belonging to **ZIF-90-Rhn** (a) changed and formed new peaks at 1726 cm<sup>−1</sup>, 1630 cm<sup>−1</sup>, 1200 cm<sup>−1</sup> and 1600 cm<sup>−1</sup> (Fig. 2, left). This indicated that **ZIF-90-Rhn** was generated by the abovementioned one-pot route *in situ* from ICA, Rhn and Zn<sup>2+</sup>.

Similarly, the aldehydic carbonyl of **ZIF-90** appeared at 1671 cm<sup>−1</sup>, and the shifts of carbonyl (–COOH, –RN–CO) and thione (–C=S) of Rhn appeared at 1720 cm<sup>−1</sup>, 1624 cm<sup>−1</sup> and 1197 cm<sup>−1</sup>. However, the characteristic peaks of carbonyl (–COOH, HN–CO), thione (–C=S) and C=C groups belonged to **ZIF-90-Rhn** (b) changed and formed new peaks in 1721 cm<sup>−1</sup>, 1614 cm<sup>−1</sup>, 1200 cm<sup>−1</sup> and 1600 cm<sup>−1</sup>, which indicated that Rhn had successfully post-modified to **ZIF-90**, and **ZIF-90-Rhn** (b) had been generated by the abovementioned post-modified tactics (Fig. 2, middle).

For organic **ligand 1**, the peaks of carbonyl (–COOH, HN–CO), thione (–C=S) and C=C groups appeared at 1733 cm<sup>−1</sup>, 1620 cm<sup>−1</sup>, 1194 cm<sup>−1</sup> and 1605 cm<sup>−1</sup>, respectively, all of which are attributed to the condensation reaction of ICA and Rhn. The peaks of carbonyl (–COOH, HN–CO), thione (–C=S) and C=C groups belonging to **ZIF-90-Rhn** (c) changed and newly shifted to 1703 cm<sup>−1</sup>, 1620 cm<sup>−1</sup>, 1200 cm<sup>−1</sup> and 1605 cm<sup>−1</sup> (Fig. 2, right), which indicated that **ZIF-90-Rhn** (c) had been generated from the organic **ligand 1** and Zn<sup>2+</sup> by the abovementioned pre-modified synthesis. It was not difficult to observe that the FT-IR results of **ZIF-90-Rhn** (a–c) were consistent, indicating that the chemical structure of **ZIF-90-Rhn** (a–c) was consistent, and there was the same original morphology between **ZIF-90-Rhn** and **ZIF-90**.

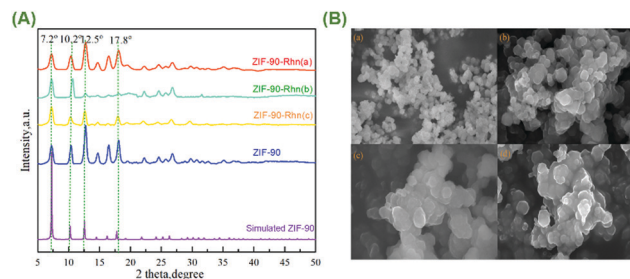


**Fig. 3** (A) PXRD data of **ZIF-90-Rhn** (a–c), **ZIF-90** and the simulated pattern of **ZIF-90**. (B) (a) SEM images of **ZIF-90**; (b) SEM images of **ZIF-90-Rhn** (a); (c) SEM images of **ZIF-90-Rhn** (b); (d) SEM images of **ZIF-90-Rhn** (c).

The powder X-ray diffraction (PXRD) patterns demonstrated that the data were consistent with the simulated **ZIF-90** and **ZIF-90-Rhn** (a–c) pattern in Fig. 3(A). The sharp diffraction peaks in the PXRD pattern of **ZIF-90-Rhn** (a–c) demonstrated that not only was there an excellent crystallinity but also the same crystallographic structure was observed with the pristine **ZIF-90**.

Moreover, the morphology characterization of **ZIF-90** and **ZIF-90-Rhn** (a–c) was performed using scanning electron microscopy (SEM) as shown in Fig. 3(B). The data indicated that **ZIF-90** included an exceptionally uniform morphology and an extraordinary cubic close-packed structure (Fig. 3(B-a)). Although the morphology of **ZIF-90-Rhn** (a, b, c) had a slight change compared to that of **ZIF-90** because of the modification reactions, the obtained **ZIF-90-Rhn** (a, b, c) still maintained a uniform cubic structure (Fig. 3(B-b–d)). With the above-mentioned results, we could confirm that the nanomaterial **ZIF-90-Rhn** (a, b, c) had the same skeleton and morphology, and they were the same molecules.

For the purpose of determining the chemical composition and element state of **ZIF-90-Rhn**, XPS was performed as shown in Fig. 4a–f. In the XPS experiment, the samples were exposed to monochromatic X-radiation, and the properties of inner-shell electrons were to be probed. As per the spectrum of **ZIF-90-Rhn** (Fig. 4a), five kinds of elements (C, O, N, S and Zn) were detected and the C 1s emission spectrum could be divided into four main peaks, as shown in Fig. 4b. With the binding energy

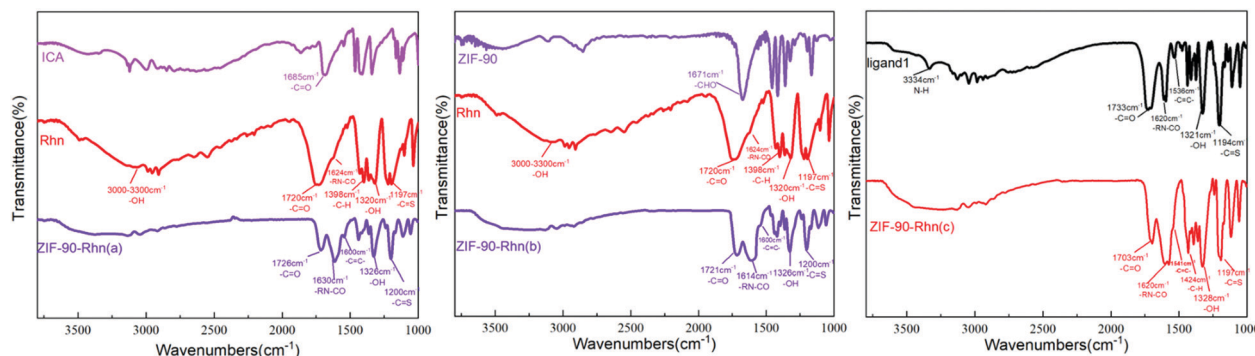


**Fig. 2** FT-IR spectra of **ZIF-90-Rhn** (a–c) and relative compounds (on the left: **ZIF-90-Rhn** (a) and relative compounds; the middle figure: **ZIF-90-Rhn** (b) and relative compounds; on the right: **ZIF-90-Rhn** (c) and relative compounds).



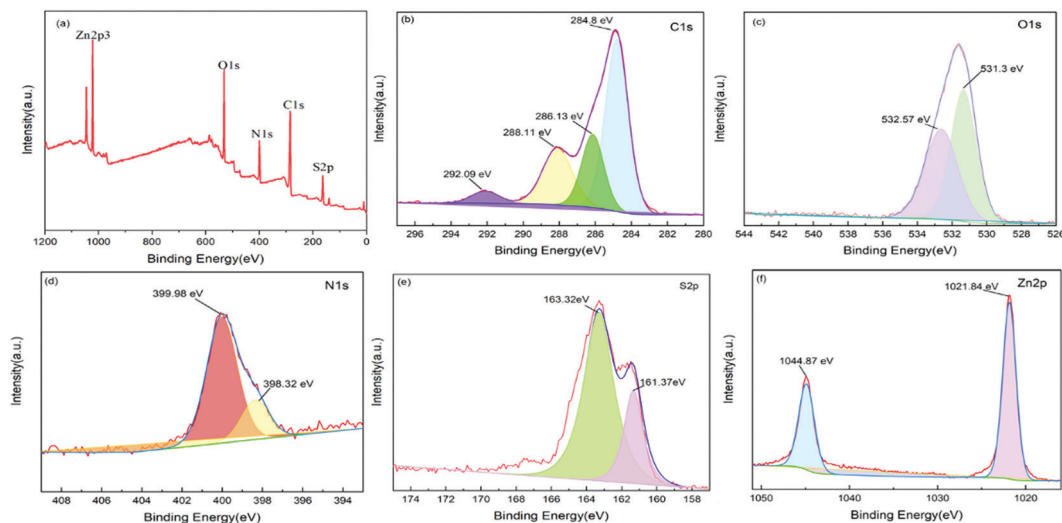


Fig. 4 XPS spectra of ZIF-90-Rhn sample: (a) the survey scan; (b) C 1s; (c) O 1s; (d) N 1s; and (e) S 2p; (f) Zn 2p.

of C 1s at 284.8 eV obtained in the XPS analysis as the reference standardized for specimen charging, three peaks with binding energies of 292.09 eV, 288.11 eV, 286.13 eV, were obtained from C–S bonds, C=O bonds and C–N bonds, respectively. The O 1s emission spectrum (Fig. 4c) could be divided into two primary peaks by the Gaussian fitting method. The peak at 531.3 eV was attributed to the –OH bonds in the organic ligand, while the peak at 532.57 eV could be attributed to C=O bonds. The N 1s emission spectrum (Fig. 4d) could be divided into two primary peaks. The peak at 399.98 eV was attributed to N–Zn bonds, while the peak at 398.32 eV was attributed to C–N bonds. The S 2p emission spectrum could be divided into two primary peaks, as shown in Fig. 4e. The binding energy at 161.37 eV was attributed to C=S bonds, while the peaks at 163.32 eV could be attributed to C–S bonds. In Fig. 4f, the Zn 2p and Zn 2p<sub>1/2</sub> spin-orbital photoelectrons were located at 1021.84 eV and 1044.87 eV, respectively. These results showed that ICA was successfully coordinated with Zn<sup>2+</sup>, and was successfully modified by the **Rhn** *in situ* synthesis method for ZIF-90-Rhn.

For checking the thermal stability, the thermogravimetric analysis (TGA) of ZIF-90-Rhn was carried out in an air atmosphere in a temperature range from 30–800 °C, as shown in Fig. S7 (ESI†). According to the TG curve, ZIF-90-Rhn displayed high thermal stability up to 156.31 °C under an air atmosphere. The first weight loss of 0.01 wt% in the temperature range of 30–156.31 °C could be attributed to the elimination of guest solvent molecules in MOF holes. The next weight loss of 18.557 wt% in the temperature of 156.31–431.85 °C could be attributed to the pentacyclic decomposition from **Rhn**. The next weight loss of 27.64 wt% in the temperature of 431.85–643.90 °C could be attributed to the pentacyclic decomposition from the ICA. After 643.90 °C, the ligand molecules were separated from the skeleton and a residue of zinc dioxide remained.

To prove permanent microporosity, we investigated the specific surface area and pore volume of the material using N<sub>2</sub> adsorption isotherm analysis. The graphs were obtained by testing the N<sub>2</sub> physical adsorption isotherms of the materials,

as shown in Fig. S8 (ESI†). The adsorption amount of ZIF-90-Rhn slowly increased and almost stopped rising after the relative pressure ( $p/p^0$ ) reached 0.98, and the material was saturated with adsorption. Brunauer–Emmett–Teller (BET) surface area was 343.767 m<sup>2</sup> g<sup>−1</sup> ( $p/p^0 = 0.30$ ), micropore volume was 0.15 cm<sup>3</sup> g<sup>−1</sup> ( $p/p^0 = 0.99$ ), and the average pore diameter was 3.55 nm. The BET test results showed that the synthesized ZIF-90-Rhn was a mesoporous nanomaterial and its pore size was suitable for the related guest molecules adsorption.

### 3.3. Fluorescence sensing and visual reading signal experiments of ZIF-90-Rhn@Cy-N

A previous report has shown that **Rhn** could recognize and coordinate Ag<sup>+</sup> to produce a **Rhn@Ag<sup>+</sup>** coordination complex.<sup>35</sup> However, in our original experiment, ZIF-90-Rhn (orange) and Ag<sup>+</sup> only produced ZIF-90-Rhn@Ag<sup>+</sup> (crimson) alone (Fig. S9, ESI†) under the recognition reaction progress. Unfortunately, neither ZIF-90-Rhn nor ZIF-90-Rhn@Ag<sup>+</sup> had fluorescence emission spectra. However, the primary objectives of the present endeavor were a one-pot synthesis of the ZIF-90-Rhn complex *in situ* and its applications as a fluorescent platform for Ag<sup>+</sup> and FA. Thus, a secondary amine dye of heptamethine cyanine (Cy-N, color was ultramarine,  $\lambda_{em} = 722$  nm) was selected and doped in the pores of ZIF-90-Rhn, which would show certain characteristics of acidity and had the ability to provide carboxyl protons due to the carboxyl group in **Rhn**. Interestingly, a grass-green new color ZIF-90-Rhn@Cy-N complex was formed when ZIF-90-Rhn (orange) was mixed with Cy-N (ultramarine), and the fluorescence of Cy-N ( $\lambda_{em} = 722$  nm) was quenched after the ZIF-90-Rhn@Cy-N complex was generated.

With the ZIF-90-Rhn@Cy-N in hand, and based on the synergism of carboxyl and thioketone groups of **Rhn**, ZIF-90-Rhn recognized and coordinated with Ag<sup>+</sup> to form ZIF-90-Rhn@Ag<sup>+</sup> with the addition of Ag<sup>+</sup>, of which the decomposition of the ZIF-90-Rhn@Cy-N complex simultaneously happened, resulting in the liberation of free Cy-N with the consequent restoration of the



fluorescent-emitting Cy-N. Finally, the recognition system shared a turn-on fluorescence due to the generation of ZIF-90-Rhn@Ag<sup>+</sup>/Cy-N, and the grass-green complex of ZIF-90-Rhn@Cy-N changed into a brick-red ZIF-90-Rhn@Ag<sup>+</sup>/Cy-N mixture with the addition of Ag<sup>+</sup> (Fig. 1).

Correspondingly, the redox activity of Ag<sup>+</sup> to FA is a well-known fact. So, a stepwise recognition detection for FA was adopted using the abovementioned new fluorescent system of ZIF-90-Rhn@Ag<sup>+</sup>/Cy-N. Indeed, when FA encountered the fluorescent system of ZIF-90-Rhn@Ag<sup>+</sup>/Cy-N, the unique redox activity between Ag<sup>+</sup> and FA resulted in a reduction reaction and transformed Ag<sup>+</sup> to Ag<sup>0</sup>. The coordination compound of ZIF-90-Rhn@Ag<sup>+</sup> was thus destroyed, and freed or restored the proton providing capacity of the functional carboxyl groups in ZIF-90-Rhn again. Therefore, the interaction between ZIF-90-Rhn and Cy-N was re-generated with the formation of the non-fluorescent ZIF-90-Rhn@Cy-N complex. The redox reaction of ZIF-90-Rhn@Ag<sup>+</sup> and FA induced a turn-off fluorescence. Moreover, a return change of the grassy green color of the ZIF-90-Rhn@Cy-N complex was followed upon the addition of FA. The foregoing results and discussion indicated that dual-signals (fluorescent signal and visual color signal) of ZIF-90-Rhn@Cy-N/Ag<sup>+</sup>/FA could be observed with this stepwise detecting of Ag<sup>+</sup> and FA (Fig. 1).

**3.3.1. Research on the influence of pH in the Ag<sup>+</sup> and FA sensing.** The effect of pH for Ag<sup>+</sup> detection was also studied. ZIF-90-Rhn@Ag<sup>+</sup>/Cy-N (100 μM) and Ag<sup>+</sup> (100 μM) were dispersed in 25 mL of methanol and sonicated for 5 min. Since the MOF structure of the probe would collapse in strong acid environment, and 100 μM Ag<sup>+</sup> would form the precipitate of AgOH when pH was above 10.3 (details shown in S1, ESI†); therefore, the fluorescent intensity was measured in a pH range of 6.0 to 10.0. Tris buffer solution and pH meter were used for the adjustment and monitoring of pH values, respectively. The results demonstrated that the pH value had little effects on the fluorescent intensity (Fig. 5a).

Similarly, ZIF-90-Rhn@Cy-N (100 μM) and FA (30 μM) were dispersed in 25 mL of methanol and sonicated for 5 min, and the fluorescent intensity was measured in a pH range from 6.0 to 10.0. The results demonstrated that pH had no obvious effects on fluorescent intensity (Fig. 5b).

**3.3.2. Sensitivity study of ZIF-90-Rhn@Cy-N for the detection of Ag<sup>+</sup>.** The fluorescence sensing detection of ZIF-90-Rhn@Cy-N for Ag<sup>+</sup>

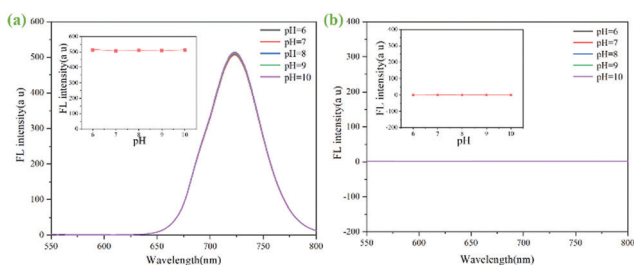


Fig. 5 (a) Fluorescence spectra changes of ZIF-90-Rhn@Cy-N (100 μM) response to Ag<sup>+</sup> (100 μM) in different pH. (b) Fluorescence spectra changes of ZIF-90-Rhn@Ag<sup>+</sup>/Cy-N (100 μM) response to FA (25 μM) in different pH.  $\lambda_{\text{ex}} = 678$  nm,  $\lambda_{\text{em}} = 722$  nm.

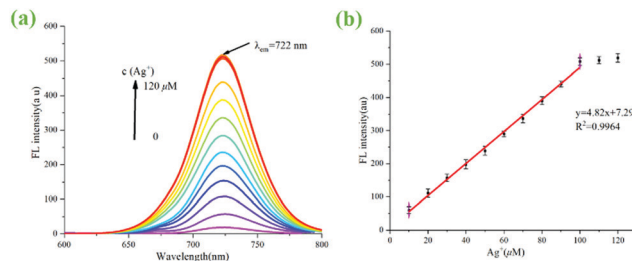


Fig. 6 (a) The fluorescence spectra of ZIF-90-Rhn@Cy-N in ethanol (100 μM) with the addition of different concentrations of Ag<sup>+</sup> (0–120 μM). (b) The linear relationship between the fluorescence intensity and Ag<sup>+</sup>.  $\lambda_{\text{ex}} = 678$  nm,  $\lambda_{\text{em}} = 722$  nm.

was investigated by titration experiments. Fluorescence spectrum studies showed that the fluorescence intensity increased gradually at  $\lambda_{\text{em}} = 722$  nm with the addition of Ag<sup>+</sup> (from 0–120 μM) under excitation of 678 nm (Fig. 6a), and a good linear relationship (10 μM to 100 μM) was obtained ( $R^2 = 0.9964$ ) (Fig. 6b). As per the formula  $L_{\text{OD}} = 3\delta/k$  ( $\delta$  is the standard deviation of the blank solution,  $k$  is the absolute value of the slope between fluorescence intensity and Ag<sup>+</sup> concentration), the detection limit was calculated to be 0.56 μM.

**3.3.3. Selectivity study of ZIF-90-Rhn@Cy-N for the detection of Ag<sup>+</sup>.** The selectivity of ZIF-90-Rhn@Cy-N for Ag<sup>+</sup> was examined and the colors (R/G value) of the probe under visible light were tested. As shown in Fig. 7a, only Ag<sup>+</sup> could change the fluorescence intensity of ZIF-90-Rhn@Cy-N, while other analytes (Ba<sup>2+</sup>, Cr<sup>3+</sup>, Cu<sup>2+</sup>, Fe<sup>3+</sup>, Hg<sup>2+</sup>, Mg<sup>2+</sup>, Mn<sup>2+</sup>, Zn<sup>2+</sup>, Hg<sup>+</sup>, Cu<sup>+</sup>, Na<sup>+</sup>, K<sup>+</sup>) could not, indicating that ZIF-90-Rhn@Cy-N had high selectivity for Ag<sup>+</sup>. The R/G values of ZIF-90-Rhn@Cy-N in different analytes are shown in Fig. 7b. The color changes of ZIF-90-Rhn@Cy-N with different analytes under visible light are shown in Fig. 7c. It was displayed that only ZIF-90-Rhn@Ag<sup>+</sup>/Cy-N showed a brick-red color.

**3.3.4. Sensitivity study of ZIF-90-Rhn@Ag<sup>+</sup>/Cy-N for the detection of FA.** The fluorescence detection titration results of FA are shown in Fig. 8a. Under  $\lambda_{\text{ex}} = 678$  nm, the fluorescence intensity of the ZIF-90-Rhn@Ag<sup>+</sup>/Cy-N system gradually decreases at  $\lambda_{\text{em}} = 722$  nm with the addition of FA (0–30 μM). A good linear relationship (1 μM to 25 μM) was obtained by fitting the fluorescence intensity in Fig. 8b ( $R^2 = 0.9982$ ),  $L_{\text{OD}} = 2.16$  μM was calculated by the same method as above. It could

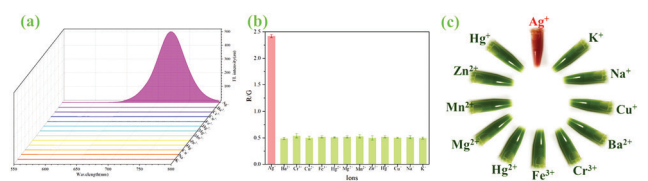
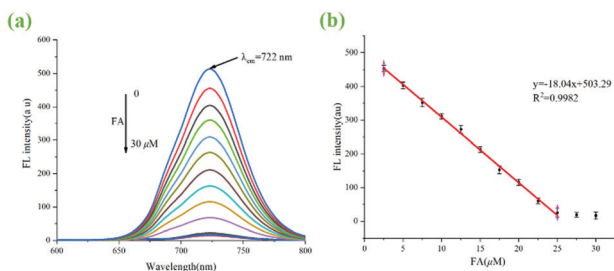


Fig. 7 (a) Fluorescence intensity of ZIF-90-Rhn@Cy-N in ethanol (100 μM) in different analytes (Ag<sup>+</sup>, Ba<sup>2+</sup>, Cr<sup>3+</sup>, Cu<sup>2+</sup>, Fe<sup>3+</sup>, Hg<sup>2+</sup>, Mg<sup>2+</sup>, Mn<sup>2+</sup>, Zn<sup>2+</sup>, Hg<sup>+</sup>, Cu<sup>+</sup>, Na<sup>+</sup>, K<sup>+</sup> was 100 μM respectively). (b) R/G values of ZIF-90-Rhn@Cy-N in ethanol (100 μM) with different analytes. (c) The color changes of ZIF-90-Rhn@Cy-N in ethanol (100 μM) in different analytes.  $\lambda_{\text{ex}} = 678$  nm,  $\lambda_{\text{em}} = 722$  nm.







**Fig. 8** (a) The fluorescence spectra of **ZIF-90-Rhn@Ag<sup>+</sup>/Cy-N** in ethanol (100 μM/100 μM) with the addition of different concentrations of FA (0–30 μM). (b) The linear relationship between the fluorescence intensity and FA concentration.  $\lambda_{\text{ex}} = 678 \text{ nm}$ ,  $\lambda_{\text{em}} = 722 \text{ nm}$ .

be seen from the experimental results that **ZIF-90-Rhn@Ag<sup>+</sup>/Cy-N** was a sensitive multifunctional probe system.

**3.3.5. Selectivity study of ZIF-90-Rhn@Ag<sup>+</sup>/Cy-N for the detection of FA.** The selectivity of **ZIF-90-Rhn@Ag<sup>+</sup>/Cy-N** for FA was examined. The effects of different analytes on the fluorescence intensity and the color (R/G value) of the probe under visible light were tested. As shown in Fig. 9a, only FA could change the fluorescence of the **ZIF-90-Rhn@Ag<sup>+</sup>/Cy-N**, while other analytes (acetaldehyde (ACE), trichloroacetaldehyde (Chloral), acetamide ( $\text{C}_2\text{H}_5\text{NO}$ ), acrylonitrile (AN), trichloromethane ( $\text{CH}_3\text{Cl}$ ), diethanolamine (DEA)) formic acid ( $\text{HCOOH}$ ), methanol ( $\text{CH}_3\text{OH}$ ) could not, indicating that **ZIF-90-Rhn@Ag<sup>+</sup>/Cy-N** was highly selective for FA. Moreover, the same results could be observed according to the R/G value as shown in Fig. 9b. The color changes of **ZIF-90-Rhn@Ag<sup>+</sup>/Cy-N** with different analytes under visible light are shown in Fig. 9c. Therefore, the high selectivity indicated that **ZIF-90-Rhn@Ag<sup>+</sup>/Cy-N** could be used as an effective probe system for the identification and detection of FA.

**3.3.6. The color (R/G value) tests of ZIF-90-Rhn@Cy-N for Ag<sup>+</sup> sensing and ZIF-90-Rhn@Ag<sup>+</sup>/Cy-N for FA sensing under visible light.** A smartphone and a spectrophotometer formed a portable detection platform to test the color changes of **ZIF-90-Rhn@Cy-N** for Ag<sup>+</sup> sensing and **ZIF-90-Rhn@Ag<sup>+</sup>/Cy-N** for FA sensing under visible light, which connected to a smartphone by Bluetooth online. As could be seen from Fig. 10a, with the addition of different concentrations of Ag<sup>+</sup> to **ZIF-90-Rhn@Cy-N**, or FA to **ZIF-90-Rhn@Ag<sup>+</sup>/Cy-N**, the color of the samples

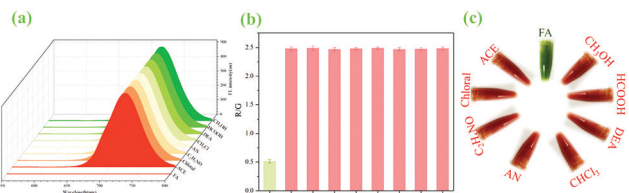


**Fig. 9** (a) Fluorescence intensity of **ZIF-90-Rhn@Ag<sup>+</sup>/Cy-N** in ethanol (100 μM/100 μM) in different analytes (FA, acetaldehyde (ACE), trichloroacetaldehyde (Chloral), acetamide ( $\text{C}_2\text{H}_5\text{NO}$ ), acrylonitrile (AN), trichloromethane ( $\text{CH}_3\text{Cl}$ ), diethanolamine (DEA), formic acid ( $\text{HCOOH}$ ), methanol ( $\text{CH}_3\text{OH}$ ), 25 μM respectively). (b) R/G values of **ZIF-90-Rhn@Ag<sup>+</sup>/Cy-N** in ethanol (100 μM/100 μM) with different analytes. (c) The color changes of **ZIF-90-Rhn@Ag<sup>+</sup>/Cy-N** in ethanol (100 μM/100 μM) in different analytes.  $\lambda_{\text{ex}} = 678 \text{ nm}$ ,  $\lambda_{\text{em}} = 722 \text{ nm}$ .

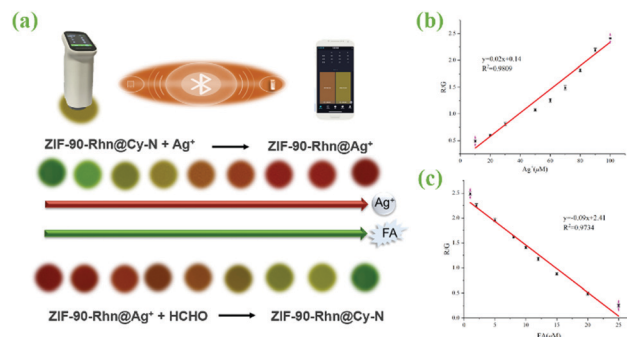


**Fig. 10** (a) The RGB analysis for the color changes of **ZIF-90-Rhn@Cy-N** in ethanol (100 μM) corresponding to Ag<sup>+</sup> (10–100 μM) and **ZIF-90-Rhn@Ag<sup>+</sup>/Cy-N** in ethanol (100 μM/100 μM) to FA (1–25 μM) using the smartphone and spectrophotometer portable detection platform. (b) The linear relationship between the R/G values and the Ag<sup>+</sup> concentrations in RGB analysis. (c) The linear relationship between the R/G values and the FA concentrations in RGB analysis.

displayed a series of changes. Then, the ColorMeter APP on the smartphone analyzed the color of the samples and produced an output of the corresponding values of R (red), G (green) and B (blue). Interestingly, the R/G value was correlated with the concentration of Ag<sup>+</sup> and FA. In the Ag<sup>+</sup> titration experiment, by linear fitting of nine data sets in the range of 10–100 μM, there was a good linear relationship between R/G value and Ag<sup>+</sup> concentration ( $R^2 = 0.9809$ ),  $L_{\text{OD}}$  was calculated to be 0.76 μM (Fig. 10b). In the titration experiment of FA, through linear fitting of nine data sets within the range of 1–25 μM, a good linear relationship existed between R/G value and FA concentration ( $R^2 = 0.9734$ ),  $L_{\text{OD}}$  was calculated to be 2.27 μM (Fig. 10c). The smartphone platform could realize real-time and online detection of Ag<sup>+</sup> and FA with high sensitivity (Tables 1 and 2).

**3.3.7. Time-dependence of the fluorescence intensity and the visibility of color.** For the time-dependence study, Ag<sup>+</sup> (3 mL, 100 μM) was added to the ethanol suspension of **ZIF-90-Rhn@Cy-N** (3 mL, 100 μM). The emission intensity at 722 nm

**Table 1** The concentrations of Ag<sup>+</sup> in the sample by fluorescence method and colorimetric method

Sample (μM)	Fluorescence method (μM)	Colorimetric method (μM)	RSD ( $n = 3$ ) (%)
20.0	20.2	20.3	0.76
30.0	30.1	29.9	0.33
50.0	49.5	50.1	0.64
80.0	80.2	80.3	0.19

**Table 2** The concentrations of FA in samples by the fluorescence method and colorimetric method

Sample (μM)	Fluorescence method (μM)	Colorimetric method (μM)	RSD ( $n = 3$ ) (%)
1.0	1.1	1.1	5.59
10.0	9.9	10.2	1.52
15.0	14.5	15.1	2.16
20.0	19.8	19.9	0.5



was obtained from 30 s to 600 s and  $\lambda_{\text{ex}} = 678$  nm (Fig. 11a). The color changes at different moments were recorded (Fig. 11b). The fluorescence intensity increased gradually with time and reached a stable level after about 3 min. While the color did not change, making clear that the best responding time was 3 min, and indicated that **ZIF-90-Rhn@Cy-N** was a fast detection probe for  $\text{Ag}^+$ .

At the time of 600 s instantaneously, FA (25  $\mu\text{M}$ ) was added. The emission intensity at 722 nm was collected from 630 s to 1200 s (Fig. 11a) and the color changes at different moments were recorded (Fig. 11c). The fluorescence intensity decreased gradually with time and reached a stable level after about 5 min, which showed that the best responding time of **ZIF-90-Rhn@Ag<sup>+</sup>/Cy-N** to FA was 5 min. This indicated that **ZIF-90-Rhn@Cy-N** could be used in a stepwise detection for  $\text{Ag}^+$  and for FA based on **ZIF-90-Rhn@Ag<sup>+</sup>/Cy-N**.

**3.3.8 The recycling of ZIF-90-Rhn@Cy-N for the detection of Ag<sup>+</sup> and FA.** The recycling experiments were conducted to realize the reuse of the **ZIF-90-Rhn@Cy-N** for detecting  $\text{Ag}^+$  and FA. As described in Fig. 1a, **ZIF-90-Rhn@Cy-N** would form **ZIF-90-Rhn@Ag<sup>+</sup>/Cy-N** product after reacting with  $\text{Ag}^+$ , and subsequently form **ZIF-90-Rhn@Cy-N'** product again after the reaction with FA. Thus, we could obtain the pure **ZIF-90-Rhn@Cy-N'** product by centrifugal operation (4000 rpm, 5 min) for the recycling experiments.

The **ZIF-90-Rhn@Cy-N'** product was employed to detect  $\text{Ag}^+$  and FA by the same methods as described in section 2.2.8, and this process was repeated for three recycles. It could be seen in Fig. 12 that **ZIF-90-Rhn@Cy-N'** was able to detect  $\text{Ag}^+$  and FA; after three recycles, the response time was still kept at 3 min and 5 min, respectively, which demonstrated that probe **ZIF-90-Rhn@Cy-N** could be reused for the detection of  $\text{Ag}^+$  and FA.

### 3.4. The sensing mechanism of Ag<sup>+</sup> and FA

The redox activity of  $\text{Ag}^+$  to FA is a well-known fact. However, the interaction between FA and  $\text{Ag}^+$  is often ignored due to the environmental and biological hazards of  $\text{Ag}^+$ .<sup>13</sup> With the functionalized **ZIF-90-Rhn** that was generated by one-pot synthesis *in situ*, pre-modification, or post-modification synthesis, a secondary amine dye of heptamethine cyanine **Cy-N** was encapsulated into the

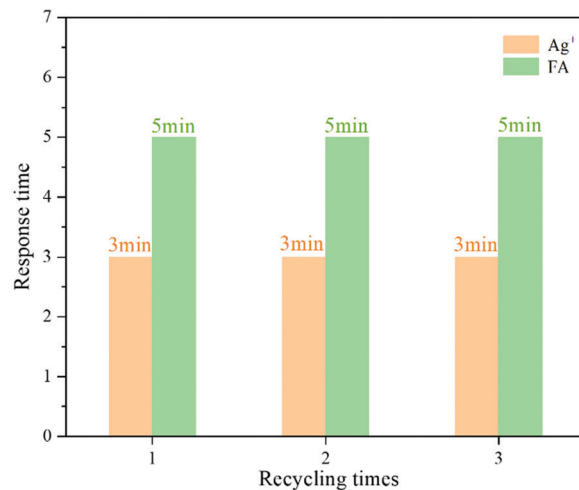


Fig. 12 The response time of **ZIF-90-Rhn@Cy-N'** product for the detection of  $\text{Ag}^+$  and FA with three recycles.

pores of this mesoporous nanomaterial. **ZIF-90-Rhn** should display certain characteristics of acidity and has the ability to provide carboxyl protons due to the carboxyl groups in **Rhn**. So, the driving force of encapsulation was the interaction between carboxyl groups in **Rhn** and secondary amine groups in **Cy-N**. It was interesting that the NIR heptamethine cyanine dye of **Cy-N** could be quenched by **ZIF-90-Rhn**. We considered that it was an ICT mechanism and the pore steric hinders of MOFs materials to NIR **Cy-N** inducing the fluorescent quenching for the ion pair complex of the non-fluorescence **ZIF-90-Rhn@Cy-N**. Depending on the strong coordination ability of S and  $-\text{COOH}$  with  $\text{Ag}^+$ , **ZIF-90-Rhn@Ag<sup>+</sup>** formed upon the addition of  $\text{Ag}^+$ , and the coordination reaction destroyed the ion-pair complex of the non-fluorescence **ZIF-90-Rhn@Cy-N**. The simultaneous decomposition of **ZIF-90-Rhn@Cy-N** induced the release of free **Cy-N**, and the system of **ZIF-90-Rhn@Ag<sup>+</sup>/Cy-N** shared a turn-on fluorescence with the addition of  $\text{Ag}^+$ .

When FA encountered the new system of **ZIF-90-Rhn@Ag<sup>+</sup>/Cy-N**, the unique redox activity of FA would induce a reduction reaction to **ZIF-90-Rhn@Ag<sup>+</sup>**, and transformed  $\text{Ag}^+$  to  $\text{Ag}^0$ . Thus, the redox would destroy the coordination compound of **ZIF-90-Rhn@Ag<sup>+</sup>** and free or restore the proton providing capacity of carboxyl functional groups in **ZIF-90-Rhn** again. The new combination of **ZIF-90-Rhn** and **Cy-N** resulted in the rebuilding of the non-fluorescent **ZIF-90-Rhn@Cy-N** complex again. With the addition of FA, the system of **ZIF-90-Rhn@Cy-N/Ag<sup>0</sup>** showed a turn-off fluorescence.

A series of interesting visual color changes were accompanied by the mentioned stepwise detection of  $\text{Ag}^+$  and FA. A new grass-green complex of **ZIF-90-Rhn@Cy-N** was produced as **ZIF-90-Rhn@Ag<sup>+</sup>/Cy-N** (orange) was mixed with **Cy-N** (ultramarine). With the addition of  $\text{Ag}^+$ , the grass-green complex of **ZIF-90-Rhn@Cy-N** changed into a new brick-red **ZIF-90-Rhn@Ag<sup>+</sup>/Cy-N** mixture, and a return color change was followed after the addition of FA. By the doped complex of **ZIF-90-Rhn@Cy-N** from **ZIF-90-Rhn** and NIR **Cy-N**, the stepwise detecting of **ZIF-90-Rhn@Cy-N** to  $\text{Ag}^+$  and **ZIF-90-Rhn@Ag<sup>+</sup>/Cy-N** mixture to FA was fulfilled, and dual-signals

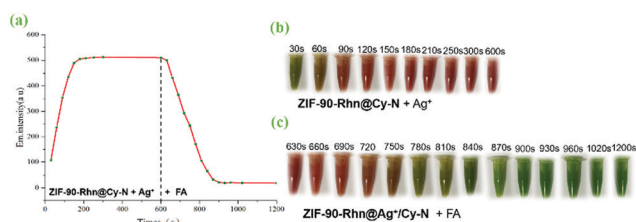


Fig. 11 Time course signaling of **ZIF-90-Rhn@Cy-N** in ethanol (100  $\mu\text{M}$ ) by  $\text{Ag}^+$  (100  $\mu\text{M}$ ) and the stepwise detecting for FA (25  $\mu\text{M}$ ) based on **ZIF-90-Rhn@Ag<sup>+</sup>/Cy-N** in ethanol (100  $\mu\text{M}$ /100  $\mu\text{M}$ ). (a) The changes in emission intensity of **ZIF-90-Rhn@Cy-N** for  $\text{Ag}^+$  sensing and **ZIF-90-Rhn@Ag<sup>+</sup>/Cy-N** for FA sensing at different time. (b) The color changes of **ZIF-90-Rhn@Cy-N** in ethanol (100  $\mu\text{M}$ ) for  $\text{Ag}^+$  at different time. (c) The color changes of **ZIF-90-Rhn@Ag<sup>+</sup>/Cy-N** in ethanol (100  $\mu\text{M}$ /100  $\mu\text{M}$ ) for FA at different time.  $\lambda_{\text{ex}} = 678$  nm,  $\lambda_{\text{em}} = 722$  nm.





(fluorescent signals and visual color signals were observed (Fig. 13).

The theoretical calculation used the B3LYP/6-31G(d) basis set in the Gaussian 09 package was adopted to explain the absorption spectra changes in the abovementioned stepwise detection (Fig. 14). Based on the density functional theory, the structure of **ZIF-90-Rhn**, **ZIF-90-Rhn@Cy-N** and **ZIF-90-Rhn@Ag<sup>+</sup>** were optimized by Gaussian software to calculate the energy difference between HOMO and LUMO, so as to determine the influence of compound changes on the spectral properties. After **ZIF-90-Rhn** was combined with **Cy-N** dye, the energy difference of HOMO–LUMO changed from 3.09 eV to 2.73 eV, indicating that the energy gap band was smaller. The position of the maximum absorption peak changed from 400 nm to 640 nm, and a large degree of red shift occurred. The color changed from orange (**ZIF-90-Rhn**) to grass-green (**ZIF-90-Rhn@Cy-N**). When **ZIF-90-Rhn@Ag<sup>+</sup>** was formed, the energy difference between HOMO and LUMO changed from 0.33 eV to 2.73 eV, and the energy gap band became larger. At this time, the maximum absorption peak of **ZIF-90-Rhn@Ag<sup>+</sup>** was at 480 nm, the color turned to brick-red of **ZIF-90-Rhn@Ag<sup>+</sup>/Cy-N** mixture. The phenomena of red shifts and blue shifts were consistent with the actual spectra, as shown in Fig. S10 (ESI<sup>†</sup>).

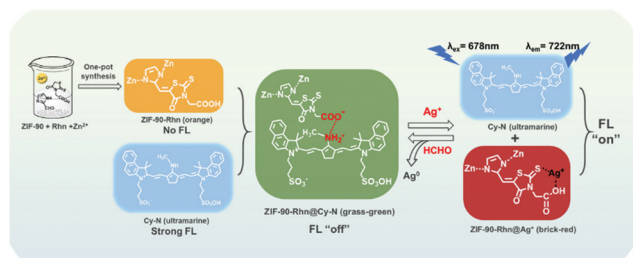


Fig. 13 Schematic illustration of **ZIF-90-Rhn@Cy-N** structure and visual detection principle for **Ag<sup>+</sup>** and **FA**.

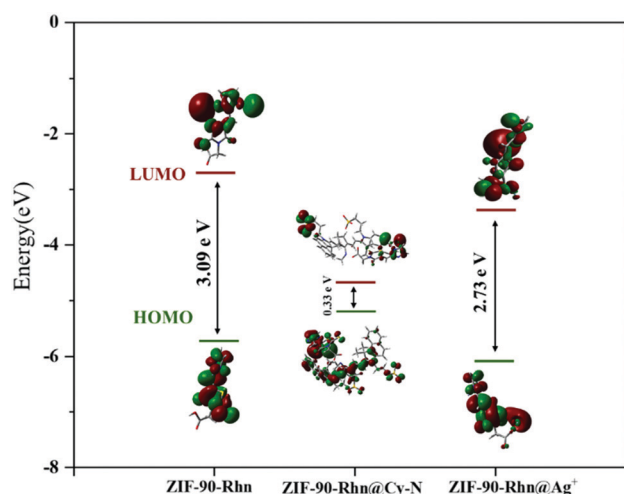


Fig. 14 Molecular amplitude plots of HOMO and LUMO of related compounds calculated using the B3LYP/6-31G(d) basis set.

To further study the mechanism of recognition and coordination mechanism of **Ag<sup>+</sup>** and **ZIF-90-Rhn**, FT-IR spectra and XPS analysis of **ZIF-90-Rhn@Ag<sup>+</sup>** were carried out (Fig. 15). FT-IR spectra of **ZIF-90-Rhn** showed that the peaks of **–CO–OH** appeared in 3000–3300 cm<sup>–1</sup>, 1320 cm<sup>–1</sup>, and the peaks of carbonyl (**–COOH**, **HN–CO**), **–C=C** and thione (**–C=S**) appeared in 1726, 1630, 1600, 1200 cm<sup>–1</sup> (Fig. 15A-a). The peaks of **–OH** and carbonyl (**–COOH**, **HN–CO**), **–C=C** and thione (**–C=S**) of **ZIF-90-Rhn@Ag<sup>+</sup>** were weakened, and the peaks of carbonyl (**–COOH**, **HN–CO**), **C=C** and thione (**–C=S**) groups in the **ZIF-90-Rhn** molecule shifted to 1750, 1657, 1629, 1157 cm<sup>–1</sup> due to the coordination of **Ag<sup>+</sup>** to **ZIF-90-Rhn** (Fig. 15A-b).

The XPS analysis of **ZIF-90-Rhn@Ag<sup>+</sup>** shows that there was the appearance of **Ag 3d** orbitals, which proved that **Ag<sup>+</sup>** had been successfully coordinated with **S** and **O** (Fig. 15B-a). The spin-orbit photoelectrons of **Ag 3d<sub>3/2</sub>** and **Ag 3d<sub>5/2</sub>** were located at 367.98 eV and 373.98 eV, respectively (Fig. 15B-b). In Fig. 15B-c, the emission spectrum of **S 2p** could be divided into two main peaks: the binding energy at 161.08 eV was attributed to the **S–Ag** bond, the binding energy at 162.18 eV was attributed to the **C=S** bond, and the binding energy at 164.08 eV was attributed to the **C–S** bond. The **O 1s** emission spectrum could be divided into three main peaks (Fig. 15B-d): binding energy of 530.6 eV of the **O–Ag** bond, peak at 531.59 because of **–OH** bond in the organic ligand, and peak at 532.5 eV because of the **C=O** bond. Moreover, it was found that the binding energy of **C=S** and **–CO–OH** from **ZIF-90-Rhn@Ag<sup>+</sup>** was slightly larger than that of **ZIF-90-Rhn** (**C=S** at 161.37 eV, **–CO–OH** at 531.3 eV), which could be attributed to the appearance of coordination bonds between **O** and **S** and **Ag<sup>+</sup>**, resulting in a decrease in electron density and an increase in the binding energy of **O** and **S**.

Moreover, after the detection reaction and the removal process of **Ag<sup>+</sup>** and **FA**, PXRD and SEM tests on recycled products of **ZIF-90-Rhn@Ag<sup>+</sup>** and **ZIF-90-Rhn@Cy-N'** were performed to confirm that the **ZIF-90**-based frameworks were not destroyed. Fig. S14a and b, (ESI<sup>†</sup>) **ZIF-90-Rhn@Ag<sup>+</sup>** and **ZIF-90-Rhn@Cy-N'** had a very regular morphology, which was similar to **ZIF-90** (Fig. S14c, ESI<sup>†</sup>). In Fig. S14d, (ESI<sup>†</sup>) it is clear that PXRDs of **ZIF-90-Rhn@Cy-N** and **ZIF-90-Rhn@Ag<sup>+</sup>/Cy-N** are consistent with the simulated **ZIF-90** pattern, and all the main diffraction peaks of **ZIF-90-Rhn@Cy-N** and **ZIF-90-Rhn@Ag<sup>+</sup>/Cy-N** at 7.2°, 10.2°, 12.5°, 17.8° demonstrated great similarity with those of the simulated **ZIF-90** pattern. All the above results confirmed that the **ZIF**-based frameworks of **ZIF-90-Rhn@Cy-N** and **ZIF-90-Rhn@Ag<sup>+</sup>/Cy-N** were not destroyed and kept intact during the detection and removal of **Ag<sup>+</sup>** and **FA**.

### 3.5. Capture of **Ag<sup>+</sup>**, **FA** in the actual samples

To evaluate the feasibility of the nano-composite **ZIF-90-Rhn** for **Ag<sup>+</sup>** capturing and removing application and the effect to **FA** in the actual stepwise procedure, a coat of chitosan non-woven fabric was made by spreading **ZIF-90-Rhn@Cy-N** evenly on its surface (1.2 mg cm<sup>–2</sup>). The functionalized non-woven fabric was cut into a circle with a diameter of 5 cm, and the films were filled into a glass column (5 cm in diameter, 20 cm in height) layer by layer. The industrial wastewater and tap water were put

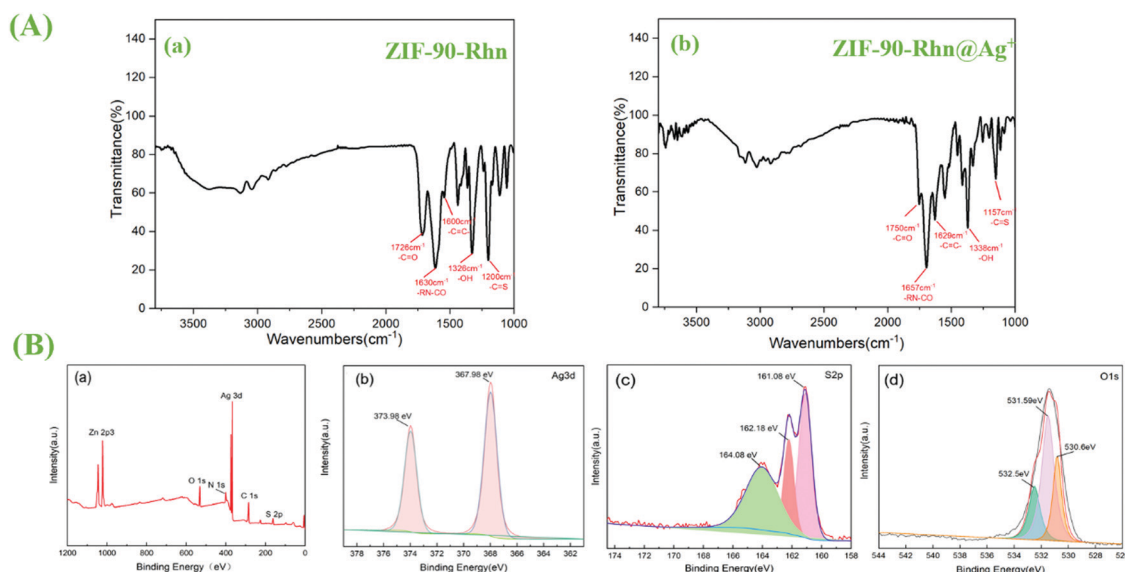


Fig. 15 (A-a) FT-IR spectra of ZIF-90-Rhn; (A-b) FT-IR spectra of ZIF-90-Rhn@Ag<sup>+</sup>; (B) XPS spectra of ZIF-90-Rhn@Ag<sup>+</sup> sample: (a) the survey scan; (b) Ag 3d; (c) S 2p; (d) O 1s.

in the filter as analytes. For a period of 5 min, the water ran through (Fig. 16a). As there was no Ag<sup>+</sup> detected in the above industrial wastewater and the tap water samples before, we added a standard solution of Ag<sup>+</sup> to it. The measurement was performed, and the recovered water was measured again. The results showed that the concentration of Ag<sup>+</sup> in the recovery water reached a discharge standard of 4.7 μM, and the drinking water content was < 0.9 μM (Table 3). Moreover, the coat colors of the functionalized non-woven fabric with ZIF-90-Rhn@Cy-N had changed from grass-green to brick-red color, meaning some complexity of ZIF-90-Rhn@Ag<sup>+</sup>/Cy-N was generated.

Then, the removal application of FA was performed in a subsequent stepwise operation. By using the above set, the blank water samples, which had been added a constant concentration of FA ran through the brick-red color filter layers for 5 min (Fig. 16b). The results showed that the removal rate of FA was above 98% (Table 4), and the coat colors of the functionalized non-woven fabric rechanged a reverse color, showing FA had been filtered out. With the description above, ZIF-90-Rhn@Cy-N exhibited certain reliability and practicability in detecting or capturing Ag<sup>+</sup> in water. Detecting or capturing of FA could also

Table 3 Removal rate of Ag<sup>+</sup> in industrial wastewater and drinking water samples by ZIF-90-Rhn@Cy-N

Real sample	Removal rate (%)	Concentration of Ag <sup>+</sup> (μM)	
		Initial	Final
Industrial wastewater	96	5.0	0.2
	96	7.0	0.3
Tap water	100	1.0	0
	97	2.0	0.06

Table 4 Removal rate of FA samples by ZIF-90-Rhn@Ag<sup>+</sup>/Cy-N

Real sample	Removal rate (%)	Concentration of FA (μM)	
		Initial	Final
Formaldehyde solution	98	3.0	0.06
	98	5.0	0.09

be achieved some satisfactory results with a stepwise variation of ZIF-90-Rhn@Ag<sup>+</sup>/Cy-N. Furthermore, the recycling of ZIF-90-Rhn@Cy-N for the removal of Ag<sup>+</sup> and FA was explored as well, and the results are described in Fig. S15 (ESI<sup>†</sup>). The good results confirmed that ZIF-90-Rhn@Cy-N could realize the recycling use for removal of Ag<sup>+</sup> and FA.

## 4. Conclusions

In conclusion, we designed, synthesized and characterized a new functionalized nanomaterial of ZIF-90-Rhn using one-pot strategic construction for *in situ* synthesis, and the post-modification of MOFs or the pre-modification of ligands synthesis method were procured, respectively, to confirm the chemical structure and the morphology of ZIF-90-Rhn. With the encapsulating of cyanine dye

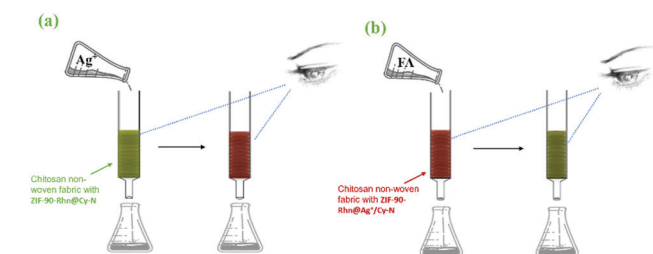


Fig. 16 (a) Schematic for the sensing and capturing of ZIF-90-Rhn@Cy-N toward Ag<sup>+</sup> in real samples. (b) The schematic for the sensing and capturing of ZIF-90-Rhn@Ag<sup>+</sup>/Cy-N toward FA in real samples.



of Cy-N to ZIF-90-Rhn, a multi-functional complex of ZIF-90-Rhn@Cy-N was successfully obtained, which could detect and capture  $\text{Ag}^+$  and FA by stepwise redox recognition reactions from the intermedial complex of ZIF-90-Rhn@ $\text{Ag}^+$ /Cy-N in dual-signals (fluorescence signals and visual color signals) in an aqueous solution. While a smartphone and a spectrophotometer formed a portable detection platform to test the color changes of ZIF-90-Rhn@Cy-N for  $\text{Ag}^+$  and ZIF-90-Rhn@ $\text{Ag}^+$ /Cy-N for FA sensing under visible light. The platform could connect a smartphone by Bluetooth online. More importantly, the above online results of the portable detection platform are consistent with the fluorescence sensing detection for  $\text{Ag}^+$  and FA. Moreover, using a chitosan non-woven fabric spread on which there was ZIF-90-Rhn@Cy-N coat evenly deposited on the surface, the feasibility of the nano-composite ZIF-90-Rhn for  $\text{Ag}^+$  capturing and removing the application, and the effect of ZIF-90-Rhn@ $\text{Ag}^+$ /Cy-N on FA in actual stepwise procedure was evaluated. The results showed that ZIF-90-Rhn@Cy-N exhibited certain reliability and practicability in stepwise detecting or capturing  $\text{Ag}^+$  and FA from water.

## Author contributions

Xiaoyu Du: conceptualization, writing – original draf. Mengwen Li: validation. Man Du: conceptualization. Xiaohui Hao: investigation. Ao Shen: project administration. Lala Hou: software. Shufeng Ma and Jiaxin Yuan: resources. Yongwei Zhao and Ziqi Li: methodology. Yunxu Yang: project administration, writing – review and editing.

## Conflicts of interest

The authors declare no competing financial interest.

## Acknowledgements

This research was supported by the National Science Foundation of China (No. 21575012), the Natural Science Foundation of Beijing (No. 2212010), and the Fundamental Research Funds for the Central Universities (FRF-BR-19-003B).

## Notes and references

- 1 Z. Yuanyuan, J. Hui and W. Xuemei, *Anal. Chim. Acta*, 2015, **870**, 1–7.
- 2 W. Su, C. Tiantian, L. Qian, L. Zhongyu and X. Song, *Optik*, 2016, **127**(2), 890–895.
- 3 J. Yuliang, K. Weiwei, S. Yongmiao and W. Bingxiang, *Tetrahedron*, 2015, **71**(34), 5584–5588.
- 4 L. Chun-Ze, A. F. Melissa, C. Rosenildo Corrêa da Costa, J. A. Gladysz, S. Andreas and B. Philippe, *Anal. Chem.*, 2010, **82**(18), 7634–7640.
- 5 B. Shiyue, S. Chao, Q. Yuting, L. Jiyang, X. Fengna and D. Xiaoping, *J. Fluoresc.*, 2016, **26**(1), 297–305.
- 6 P. D. Howe and S. Dobson, IPCS Concise International Chemical Assessment Documents 44, 2002.
- 7 Y. Xuan and W. Erkang, *Anal. Chem.*, 2011, **83**(12), 5005.
- 8 M. N. Descamps, T. Bordy, J. Hue, S. Mariano, G. Nonglaton, E. Schultz, T. H. Tran-Thi and S. Vignoud-Despond, *Procedia Eng.*, 2010, **5**, 1009–1012.
- 9 G. Xiao-Liang, C. Yan, J. Hong-Lan, Q. Xian-Bo and Y. Du-Li, *Sensors*, 2018, **18**(9), 3141.
- 10 B. Opas, D. Frank, K. Proespichaya, T. Panote and H. P. J. Seamus, *Anal. Chim. Acta*, 2010, **659**(1–2), 251–257.
- 11 S. Patrik, S. David, H. A. Tracey, S. Waleed Al and E. B. James, *Rapid Commun. Mass Spectrom.*, 1999, **13**, 1354.
- 12 K. Shuji, B. J. Patrick, K. H. Tad and B. M. Veronica, *Anal. Chem.*, 2001, **73**, 2992.
- 13 G. R. Möhlmann, *Appl. Spectrosc.*, 1985, **39**, 98–101.
- 14 J. R. Hopkins, T. Still, S. Al-Haider, I. R. Fisher, A. C. Lewis and P. W. Seakins, *Atmos. Environ.*, 2003, **37**, 2557–2565.
- 15 L. Xiaoyong, L. Peng, Y. Tianlin, T. Jinchun and X. Ping, *Scr. Mater.*, 2012, **67**, 293–296.
- 16 C. Er-Xia, Y. Hui and Z. Jian, *Inorg. Chem.*, 2014, **53**, 5411–5413.
- 17 F. Jing Mei, L. Fei, Z. Xi Juan, H. Xiao Li and L. Yuan Fang, *Analyst*, 2014, **139**, 801–806.
- 18 K. Peramaiah, P. Alagarsamy, P. Mani, K. Mariyappan and N. Bernauidshaw, *Microchim. Acta*, 2017, **184**, 2265–2273.
- 19 K. Xiang-Jing and L. Jian-Rong, *Engineering*, 2021, **7**, 1115–1139.
- 20 W. Bin, L. Xiu-Liang, F. Dawei, X. Lin-Hua, Z. Jian, L. Ming, X. Yabo, L. Jian-Rong and Z. Hong-Cai, *J. Am. Chem. Soc.*, 2016, **138**(19), 6204–6216.
- 21 H. Tao, K. Xiang-Jing and L. Jian-Rong, *Acc. Chem. Res.*, 2021, **54**, 3083–3094.
- 22 L. P. William, M. Soumya, R. D. Nathan, D. V. Aamod, L. Jing and G. K. Sujit, *Chem. Soc. Rev.*, 2017, **46**, 3242–3285.
- 23 H. Ji-Na and Y. Bing, *J. Mater. Chem. A*, 2015, **3**(9), 4788–4792.
- 24 R. Ayyanu, P. Perumal and M. Norhashimah, *ACS Appl. Mater. Interfaces*, 2018, **10**, 20550–20558.
- 25 V. Kowsalya, D. Akash, K. Ki-Hyun, B. W. Danil, K. Pawan and Y. Qu, *Sens. Actuators, B*, 2017, **241**, 938–948.
- 26 N. Soutick, S. Ena, T. Vishal and B. Shyam Biswas, *Inorg. Chem.*, 2018, **57**(24), 15149–15157.
- 27 Z. Huimin, L. Xiaojing, L. Wanze, W. Peng, C. Shuo and Q. Xie, *RSC Adv.*, 2014, **4**(69), 36444–36450.
- 28 L. Mengwen, S. Ao, L. Yueqi, Z. Hao, H. Xiaohui, L. Xueliang, S. Xinchao and Y. Yunxu, *Anal. Methods*, 2020, **12**(29), 3748–3755.
- 29 L. Mengwen, A. Shen, D. Man, H. Xiaohui, W. Hongquan, D. Xiaoyu, M. Shufeng, Y. Jiaxin and Y. Yunxu, *RSC Adv.*, 2021, **11**(54), 34291–34299.
- 30 C. Liyu, L. Rafael and L. Yingwei, *Chem. Soc. Rev.*, 2017, **46**(15), 4614–4630.
- 31 C. Liyu Chen, C. Huirong, L. Rafael and L. Yingwei, *Chem. Sci.*, 2014, **5**(10), 3708–3714.
- 32 L. Yucheng Luo, F. Shiyan, Y. Wenqian, W. Zili, C. A. David, L. Chaolun, S. Jianying and S. Chengyong, *Adv. Mater.*, 2018, **30**(6), 1704576.
- 33 H. Huajun, M. En, C. Yuanjing, Y. Jiancan, Y. Yu, S. Tao, W. Chuan-De, C. Xueyuan, C. Banglin and Q. Guodong, *Nat. Commun.*, 2016, **7**, 11087.





- 34 J. Shengye, S. Ho-Jin, F. K. Omar, W. P. Gary and H. T. Joseph, *J. Am. Chem. Soc.*, 2013, **135**(3), 955–958.
- 35 D. Xiaoping, L. Mengzhao, L. Zhanzhao, J. Axiang Jin, M. Yangde, H. Xingliang, S. Hui, W. Hai and Z. Xin, *J. Phys. Chem. C*, 2016, **120**(23), 12539–12548.
- 36 H. Huajun, C. Yuanjing, L. Bin, W. Bo, J. Chuanhong, Y. Jiancan, Y. Lijia, Y. Yu, C. Banglin and Q. Guodong, *Adv. Mater.*, 2019, **31**(6), e1806897.
- 37 L. Haibin, M. Li, Z. Liya, G. Jing, H. Zhihong, H. Ying and J. Yanjun, *Chem. Commun.*, 2018, **54**(76), 10754–10757.
- 38 T. Pichandi, D. Natarajan, K. Manikantan Syamala and E. Shanmugam, *ACS Sustainable Chem. Eng.*, 2019, **7**(11), 9865–9874.
- 39 M. William, D. J. Christian, F. Hiroyasu, B. Rahul and Y. M. Omar, *Am. Chem. Soc.*, 2008, **130**, 12626–12627.
- 40 S. Fa-Kuen, W. Shao-Chun, L. Sin-Yen and W. C.-W. Kevin, *Chem. – Eur. J.*, 2013, **19**, 11139–11142.
- 41 Z. Feng-Ming, D. Hong, Z. Xin, S. Xiao-Jun, L. Ming, Y. Dou-Dou, L. Xin Liu and W. Jin-Zhi, *ACS Appl. Mater. Interfaces*, 2017, **9**, 27332–27337.
- 42 X. Wenlei and W. Fei, *Energy Convers. Manage.*, 2019, **198**, 111922.

